JOURNAL OF MATERIALS SCIENCE 13 (1978) 972–984

Crystallite size determination and identification of lamellar surfaces of microparacrystallites for uniaxially and doubly oriented polyethylene films*

K. KAJI
Department of Polymer Chemistry, Kyoto University, Kyoto, Japan

T. MOCHIZUKI, A. AKIYAMA
Central Research Institute, Kuraray Co. Ltd., Aoeyama, Kurashiki, Japan

R. HOSEMANN
Fritz-Haber-Institut der MPG, Teilinstitut für Strukturforschung, Berlin-Dahlem, Germany

Low density polyethylene (PE) films stretched 4 x at 20° C and annealed at 100° C show the well-known SAXS four-point diagrams with a tilting angle of lamellae of 35°. The 7.5 nm thick lamellae consist of rod-like microparacrystallites (mPCs) of 25 nm x 7.2 nm lateral sizes; the long axes of the mPCs are turned around the *c*-axis by 31° from the *b*-axis. The mPCs of each lamella stack together laterally like monolayers of cigars. After rolling the molten film at room temperature and then annealing at 100° C, a doubly oriented film arises, each half of it, anterior or posterior, producing a monoclinic two-point diagram. These are superimposed in SAXS. The mPCs are oriented in the plane stress field so that their *b*-axis is orthorgonal to the stretching direction and parallel to the film surface; their long axes however are again turned as before, but now by 26°. Furthermore their *a*-axis is tilted around the *b*-axis by 8° and the lamellar basal surface tilted against the *b*-axis in the opposite direction by 40°. The line profiles of the SAXS reflections give evidence that statistical irregularities of the lamellar surfaces are correlated in the 8° tilted direction or along the chain axis with the neighbouring surfaces by means of ultrafibrillar properties of the lamellar bundles, e.g. ribbon-like microfibrillar details of the lamellae. These can be described quantitatively by applying the theory of paracrystals on the superlattice generated by the centres of the mPCs. The lamellar surfaces are approximately parallel to the {5 2 3} and {3 1 1} netplanes of mPCs for the uniaxially and doubly oriented films, respectively. The conventional theory of mesophases can never describe structures which combine lamellar and fibrillar properties.

1. Introduction

It is well known that solution- and melt-crystallized polyethylenes (PE) often have a lamellar structure. In most cases the chain molecules are tilted against the lamellar normal; the tilting angle is larger at high crystallization temperatures [1]. In cold-stretched PE the tilting angle for branched PE is larger than for linear PE [2]. This result may be due to the fact that the melting point of branched PE is lower than that of linear PE. If the cold-stretched PE is annealed with free ends, the lamellae as a whole rotate and finally become

*Dedicated to P. P. Ewald on the occasion of his 90th birthday.

© 1978 Chapman and Hall Ltd. Printed in Great Britain.

orthogonal to the stretch direction, and then the molecular chains within them remain to be tilted [2–4].

Cold-stretched materials have a more fibrillar structure and microfibrils were found by electron microscopy in stretched PE single crystals which are tightened between the cleavages. A combined analysis in two dimensions of small- and wide-angle X-ray scattering (SAXS and WAXS) with pinholes showed that the diffraction can be explained by a paracrystalline superstructure of the centres of mosaic blocks, which is intermediate between a lamellar (smectic) and fibrillar (nematic) structure [2, 5].

It is the aim of this paper to show that the superstructure of doubly oriented PE generated under plane stress gives rise to a new SAXS pattern, which can be no longer explained by a two-phase model of lamellar bundles, but gives direct evidence that there exist special statistical correlations between the surfaces of adjacent lamellae. It proves that lamellar and microfibrillar properties exist simultaneously, which forces us to introduce the concept of paracrystalline superstructures. The results do not only agree with the WAXS pattern but also give new evidence of paracrystalline mosaic blocks which contribute both to the lamellar and fibrous features of the sample.

2. Experimental

2.1. Samples

Low density polyethylene Simikathene F101-1, which was kindly supplied by Sumitomo Kagaku Kogyo Co. Ltd., Japan, was used for this work. The melt index of this bulk material is 0.3 and its degree of branching is 2.3 CH_3/100 C. The pellets of this material were melt-compressed into films and then stretched at room temperature to a draw ratio of 4. The stretched films were annealed at 100° C in air at constant length for 30 min. These films remained transparent and the density of them was 0.918 Mg m^{-3}. We call them uniaxially oriented samples. Melt-compressed films were rolled at room temperature to a draw ratio of 4 and then in the perpendicular direction to a draw ratio of 2. These rolled films were annealed at 100° C in air at constant length for 1.5 h. The annealed films were about 0.12 mm in thickness and of density 0.925 Mg m^{-3}. These were called doubly oriented samples.

WAXS and SAXS photographs of these samples were taken by Rigaku-Denki Rotoflex using Ni-filtered Cu$K\alpha$ radiation generated at 40 kV and 100 mA. Fig. 1 shows the relation of the sample position to the incident X-ray beam. X_1 is normal to the film surface of the sample and X_3 is parallel to the draw axis. X_2 is perpendicular to both X_1 and X_3. The camera distance from sample to photographic film was 400 mm for SAXS. The exposure time necessary to obtain the SAXS pattern along the X_3-axis was at least 24 h.

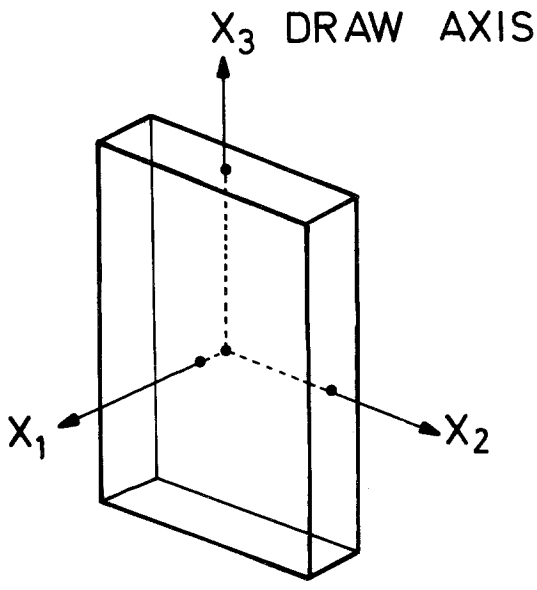

Figure 1 Coordinates for the PE film. X_1 normal to the film, X_3 stretching direction, X_2 orthogonal to X_1 and X_3.

2.2. Determination of crystallite sizes and shapes

The cross-sectional shapes of crystallites in the direction perpendicular to the chain axis were estimated with a method developed by Hosemann and his co-workers [6, 7]. Line profile analysis proves that the mosaic blocks are micropara-crystallites (mPCs). Their cross-sectional shape can be expressed by an ellipsoid of which the diameter in a given direction is proportional to the crystallite size in that direction [8].

The crystallite sizes were determined from the integral widths of WAXS reflections, according to paracrystalline theory. When the lattice distortions and shape factors are Lorentzian, the integral width of a reflection is given by;

$$\delta\beta_{hkl} = \frac{1}{\bar{D}_{hkl}} + \frac{\pi^2 g^2}{\bar{d}_{hkl}} p^2 \qquad (1)$$

where $\bar{D}_{hkl}$ is the crystallite size in the direction

normal to the $(h\,k\,l)$ lattice planes, g is the paracrystalline distortion, p is the order of the reflection, and $\bar{d}_{hkl}$ is the lattice distance. However Equation 1 is also valid for the other profiles.

The equation of the form-ellipsoid for the crystallite shape is given by;

$$\left(\frac{2}{\bar{D}_{hk0}}\right) = \left(\frac{\cos\tau}{r_1}\right)^2 + \left(\frac{\sin\tau}{r_2}\right)^2 \qquad (2)$$

where $\tau = \tau_a + \tau_b$. r_1 and r_2 are the short and long principal axes of the ellipsoid, respectively. τ_a is the angle between r_1 and the [1 0 0] axis, and τ_b is the angle between the [1 0 0] and $[h\,k\,0]$ axes (see Fig. 3). $[h\,k\,0]$ represents the direction normal to the $(h\,k\,0)$ plane. In order to fix Equation 2 it is necessary to know at least three crystallite sizes in different $[h\,k\,0]$ directions. Unfortunately for the polyethylene samples used, crystallite sizes, corrected for the distortion effect, could be obtained only in one or two $[h\,k\,0]$ directions. The calculations were carried out by applying Equation 2 until the calculated $\bar{D}_{hkl}$ values agreed reasonably with those observed in every direction. The crystallite sizes along the c-axis were measured from the 0 0 2 reflection without removal of the effect of lattice distortions, because the paracrystalline distortions in the polyethylene lattices do not affect on the chain-axial direction [9].

The line profiles of the X-ray reflections were obtained with Ni-filtered Cu$K\alpha$ radiation generated at 40 kV and 15 mA, a scintillation counter, and symmetrical transmission techniques. The intensities were measured by a point count technique; the counting period was 8000 counts at each point. Background and amorphous contributions were subtracted from the crystalline reflections as in the previously reported method [10]. Graphite was used as a standard to determine the instrumental broadening. For the doubly oriented sample, the 1 1 2 reflection and an amorphous halo were superimposed on the 0 0 2 reflection. These were removed from the 0 0 2 reflection by a usual method [11].

3. Crystallite sizes and shapes

The Tables I and II show the observed widths of the equatorial and 0 0 2 reflections for the uniaxially and doubly oriented samples respectively. For the $h\,k\,0$ and $h\,0\,0$ reflections the contributions of the crystallite size and lattice distortions can be separated according to Equation 1,

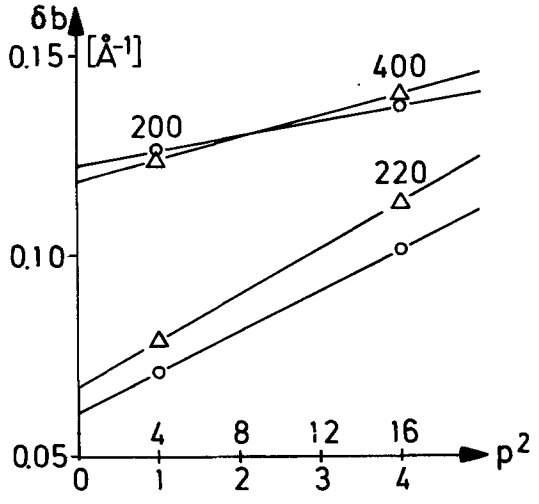

Figure 2 Plots of the integral widths of equatorial reflections against p^2 for uniaxially (○) and doubly (△) oriented PE samples; p is the order of reflection. The intercept and slope indicate the size and distortions of the microparacrystallites (mPCs) respectively.

supposing that only paracrystalline distortions are present. This is justified because the samples had been annealed after mechanical treatment. These separations were carried out as in Fig. 2; the crystallite size and lattice distortions were calculated from the intercept and the slope of the straight line respectively. The results are also listed in Tables I and II. For the other reflections the values, which are given in parentheses, were estimated when the form-ellipsoid was determined.

Fig. 3 shows the determined form-ellipsoids for the uniaxially and doubly oriented samples; their main axes are $2r_1 = 7.2$ nm, $2r_2 = 25.2$ nm for the former, and $2r_1' = 7.7$ nm, $2r_2' = 22.5$ nm for the latter. The most important fact, which is seen in

TABLE I The integral widths $\delta\beta$ of reflections, the crystallite sizes D, and paracrystalline distortions g for the uniaxially oriented sample. The values in parentheses are for a form-ellipsoid with $2r_1 = 7.2$ nm, $2r_2 = 25.2$ nm and $\tau_a = 31°$ (see Fig. 3)

$h\,k\,l$	$\delta\beta$ (nm^{-1})	$1/\delta\beta$ (nm)	$\bar{D}$ (nm)	g (%)
1 1 0	0.071	14.1	16.1	
2 2 0	0.101	9.9	16.1	$g_{110} = 2.0$
2 0 0	1.126	8.0	8.3	
4 0 0	0.137	7.3	8.3	$g_{200} = 0.6$
0 2 0	0.088	11.4	(12.6)	($g_{020} = 1.9$)
1 2 0	0.082	12.3	(14.8)	($g_{120} = 2.4$)
3 1 0	0.132	7.6	(9.7)	($g_{310} = 2.6$)
0 0 2	0.110	9.1	9.1	$g_{002} = 0$

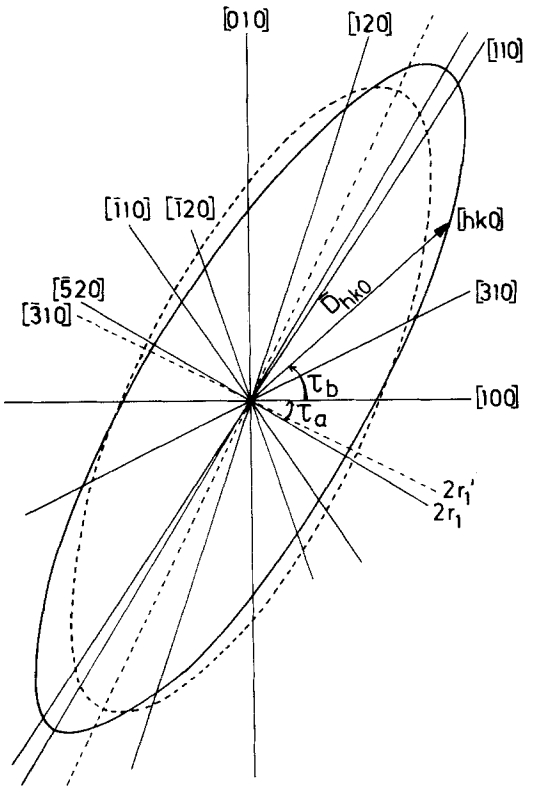

Figure 3 Form-ellipsoids of the microparacrystallites for the uniaxially and doubly oriented PE samples. ——: uniaxially, $2r_1 = 7.2$ nm, $2r_2 = 25.2$ nm, $\tau_a = 31°$; – – – –: doubly, $2r'_1 = 7.7$ nm, $2r'_2 = 22.5$ nm, $\tau'_a = 26°$.

this figure, is that the long main axis of the form-ellipsoid does not conform with the crystal b-axis as already found for the solution-grown single crystals [6, 7] and high pressure crystallized extended chain crystals [12]. The long main axes of the form-ellipsoids are inclined at 31° and 26° to the b-axis for the uniaxially and doubly oriented samples respectively. Thus the larger lateral sides of microparacrystals are the {5 2 0} and {3 1 0} planes respectively. Furthermore, the crystallite sizes for these two samples are almost identical. This means that the crystallite sizes were determined mainly by the crystallization temperature and not by the preceding mechanical treatment.

TABLE II The integral widths $\delta\beta$ of reflections, the crystallite sizes D, and paracrystalline distortions g for the doubly oriented sample. The values in parentheses are for a form-ellipsoid with $2r'_1 = 7.7$ nm, $2r'_2 = 22.5$ nm and $\tau'_a = 26°$ (see Fig. 3)

hkl	$\delta\beta$ (nm^{-1})	$1/\delta\beta$ (nm)	$\bar{D}$ (nm)	g (%)
1 1 0	0.079	12.7	14.9	
2 2 0	0.113	8.9	14.9	$g_{110} = 2.2$
2 0 0	0.124	8.1	8.5	
4 0 0	0.140	7.1	8.5	$g_{200} = 0.7$
0 2 0	0.083	12.1	(14.4)	($g_{020} = 1.8$)
1 2 0	0.066	15.2	(15.8)	($g_{120} = 0.5$)
3 1 0	–	–	(9.7)	–
0 0 2	0.124	8.1	8.1	$g_{002} = 0$
1 1 2	0.119	8.4	8.4	$g_{112} = 0$

The crystallite size along the c-axis for the doubly oriented sample can be also estimated from the 1 1 2 reflection by using the relation

$$\bar{D}_{001} = \bar{D}_{112} \cos \chi_{112} \qquad (3)$$

where χ_{112} is the angle between the {1 1 2} and {0 0 1} netplanes. The value estimated from the 1 1 2 reflection is 8.02 nm, and agrees well with that of 8.05 nm from the 0 0 2 reflection.

4. Uniaxially oriented samples

Fig. 4 shows the WAXS and SAXS patterns of the uniaxially oriented sample. It is seen from the WAXS pattern that this sample is uniaxially oriented; the patterns in the X_1- and X_2-directions are the same and that in the X_3-direction shows homogeneous rings. In the X_3-diagram a ring is seen near the incident beam, which consists of the 1 1 0 and 2 0 0 reflections created by the continuous radiation. The SAXS patterns in the X_1- and X_2-directions show the four-point diagrams with poor separation. Judging from the SAXS patterns of the doubly oriented sample, as will be shown in Fig. 7, this poor separation seems to be due to the superposition of the meridional two-point diagram and the four-point one. The "long period" along the draw or chain axis was found to be 17.0 nm. Furthermore, one can estimate the inclination angle ϕ of the normal of the crystallite basal surface to the draw axis as shown in Fig. 5; then $\tan \phi = 2h_1/2h_3$. For the present sample the inclination angle was $\phi = 35°$ so that the normal of the crystallite basal surface is inclined at 35° to the {0 0 1} plane, since the c-axis is parallel to the draw axis. The interlamellar distance is given by $17.0 \cos \phi = 14.0$ nm.

On the SAXS pattern in the X_3-direction a very diffuse reflection ring appears as shown in Fig. 4c, and its profile is given in Fig. 6. The diameter of this ring corresponds to about 9.5 nm in distance. This shows that the microparacrystals with a cross-section of 25.2 nm x 7.2 nm are packed with their longer sides in contact with each other within a lamella, like layers of cigars. This generates ribbon-like fibrillar bundles along the fibre direction X_3 with a relatively regular interfibrillar distance

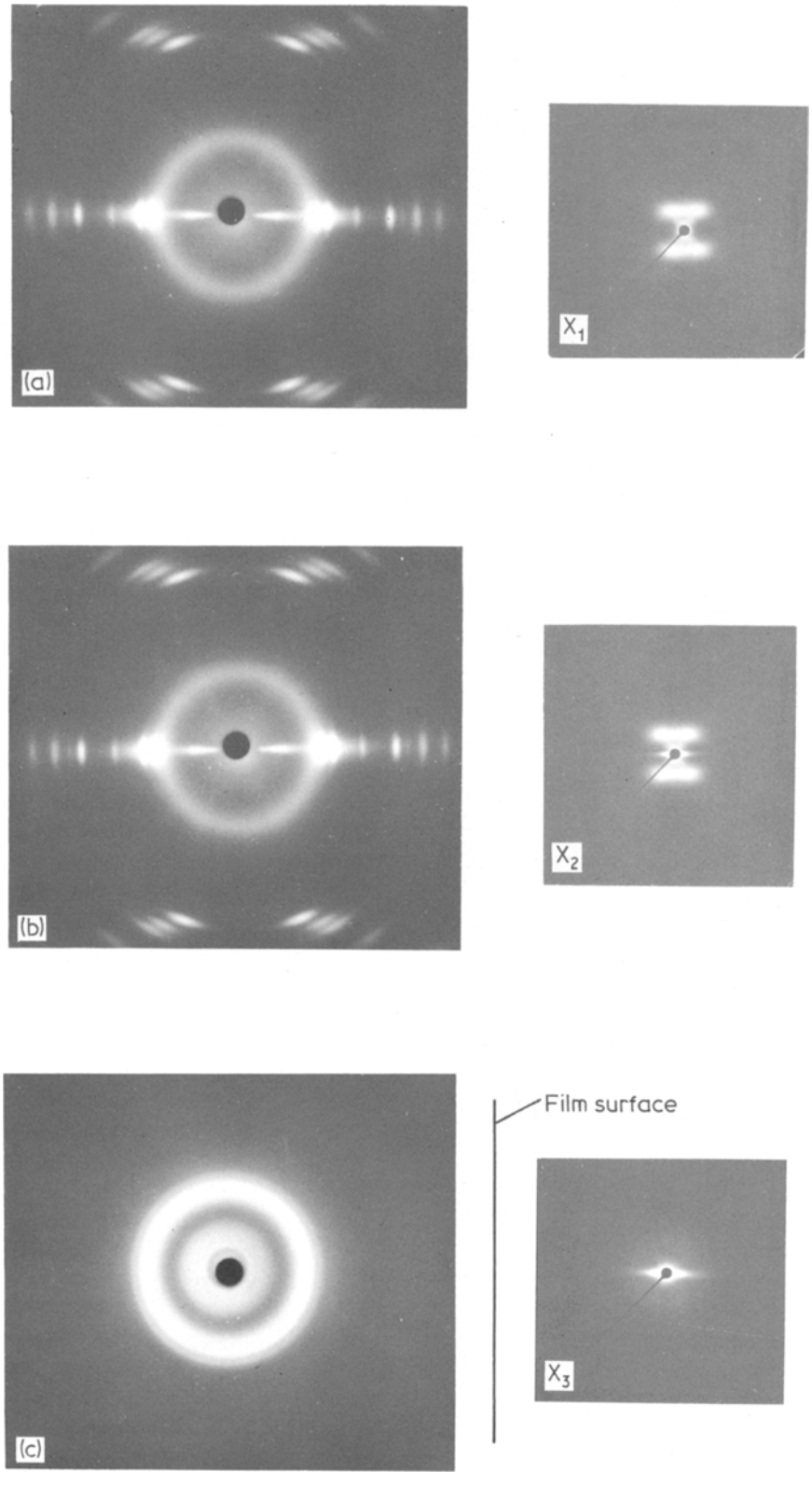

Figure 4 WAXS (on the left) and SAXS (on the right) patterns of a uniaxially oriented PE film. Incident X-ray beams are parallel to the X_1-, X_2- and X_3-axes respectively. (See Fig. 1.)

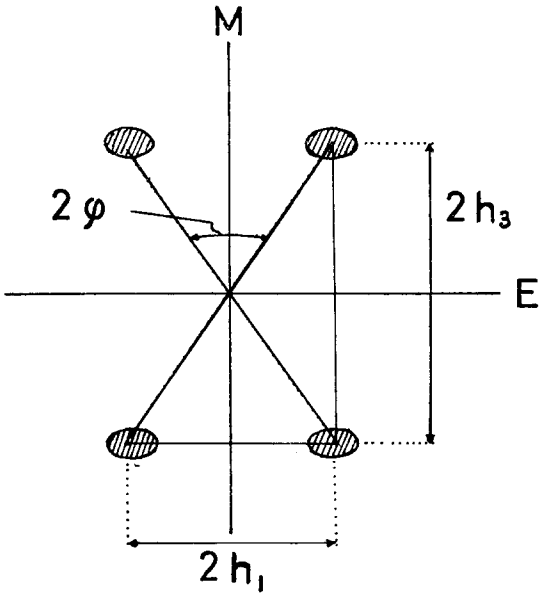

Figure 5 Definition of the angle ϕ. E = equator, M = meridian.

and inclined by $\tau_a = 31°$ against the $\{X_2X_3\}$ plane. The interference between adjacent mPCs is ring-shaped, since all orientations of the long axis are possible orthogonal to X_3. One has therefore to multiply $I(s)$ with s in Fig. 6 to find the position of the peak ($s = 4\pi \sin\theta/\lambda$). The interfibrillar distance is therefore somewhat smaller than 9.5 nm (see Fig. 16 for details).

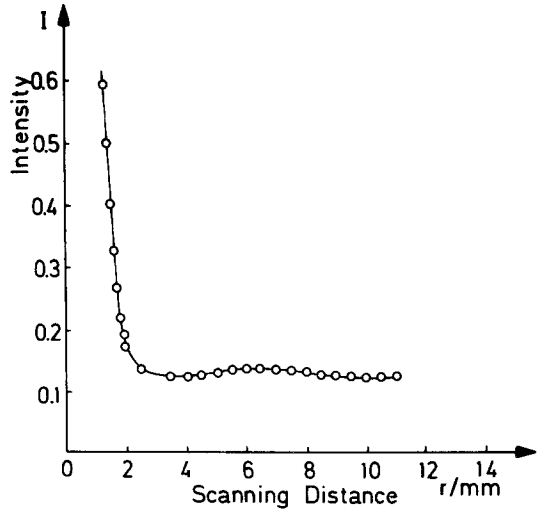

Figure 6 Profile of SAXS in the X_3-direction for the uniaxially oriented PE film (Fig. 4) which was scanned by a microdensitometer. The diffuse intensity maximum is in the vicinity of 9.5 nm.

The crystallinity is given by the interlamellar and interfibrillar distances and the sizes of the mPCs in these directions. For that one has to use the three-dimensional expression of the shape ellipsoid instead of Equation 2. This is given by;

$$\left(\frac{2}{D_{hkl}}\right)^2 = \sum_{n=1}^{3}\left(\frac{\cos\tau_n}{r_n}\right)^2 \qquad (4)$$

where τ_n is the angle between the normal of $(h\,k\,l)$ and the mean axis r_n. In our case $2r_3$ is the axis in the X_3-direction and was found to be ~8 nm; nearly the same as $2r_1'$. The shape ellipsoids of the mPCs seem to have a rotational-symmetric shape along the [1 1 0] direction. The thickness of the lamellae orthogonal to the surface is then ~7.5 nm. Taking into account the packing density of the cigar-shaped mPCs within the lamellae (>7.2/9.5) and the above calculated distance of 14 nm between the lamellae centres, one obtains a value of the order of

$$7.5/14 \times 7.2/9.5 \sim 40\% \qquad (5)$$

for the degree of crystallinity in the volume fraction. From the macroscopic density ρ of the specimen film one can also calculate the degree of crystallinity in the volume fraction arbitrarily assuming that the density ρ_a in the "amorphous phase" is the same as in molten material. Thus

$$X_{c,v} = \frac{\rho - \rho_a}{\rho - \rho_a} \sim 41\% \qquad (6)$$

where $\rho_c = 1.008$ and $\rho_a = 0.855\,\mathrm{Mg\,m^{-3}}$ are the crystalline [13] and amorphous [14] densities, respectively. The agreement between the degrees of crystallinity from the packing model and from the observed density is fortuitously good.

5. Doubly oriented samples

Fig. 7 shows the WAXS and SAXS patterns of the doubly oriented sample. The WAXS pattern in the X_3-direction shows that the {2 0 0} netplane or b-axis of crystallites is parallel to the macroscopic film surface. As seen from the WAXS pattern in the X_2-direction, the reflection 0 2 0 therefore does not appear. The {0 0 2} and the {2 0 0} netplanes are both split by about $\psi = 8°$. The c-axis of the mPCs is therefore tilted from the draw direction X_3 around the b-axis by an angle $\psi = 8°$. Thus all equatorial reflections in the X_1 pattern are not split, while all of the $h\,0\,0$ reflections in the X_2 pattern are split by an angle ψ.

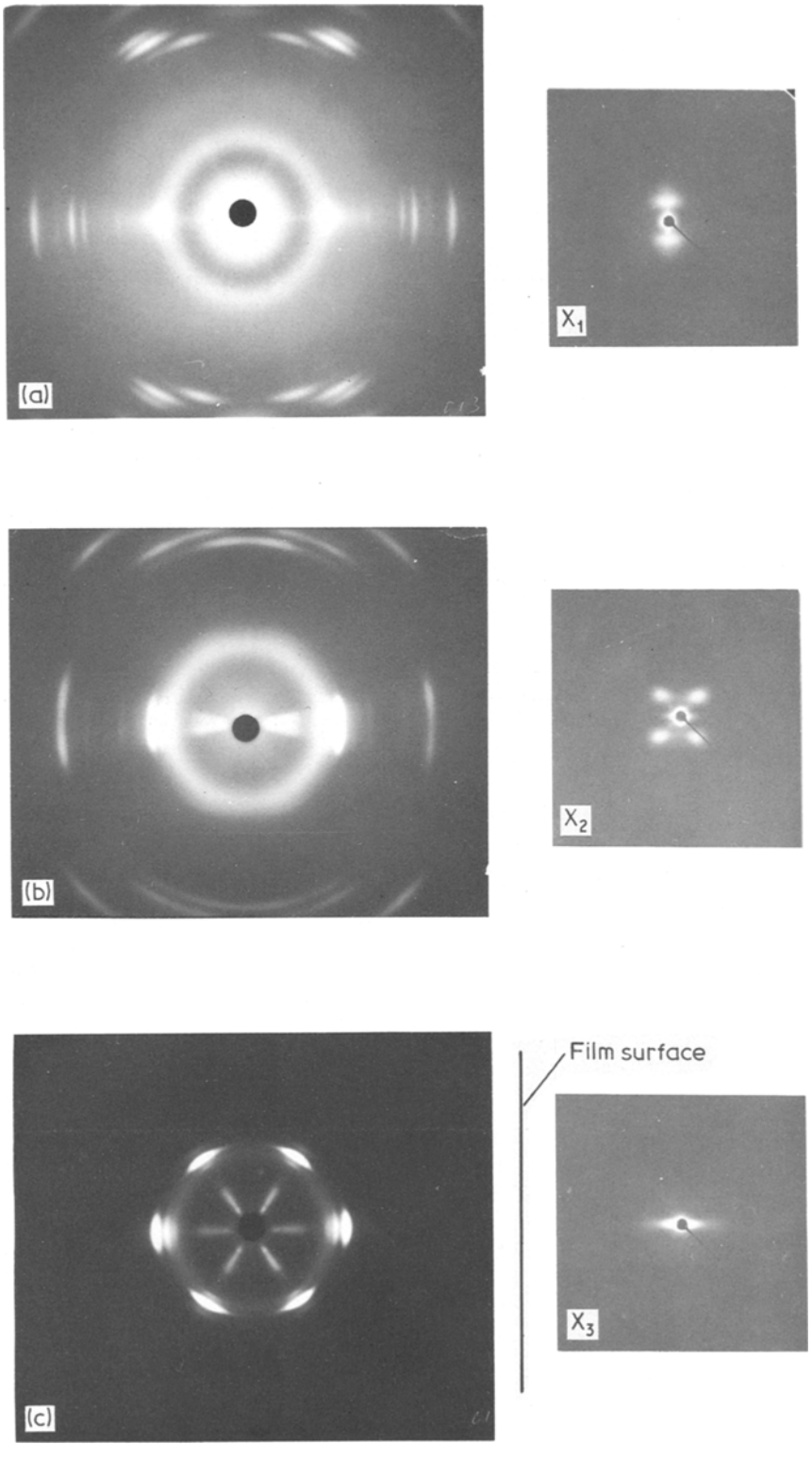

Figure 7 WAXS (on the left) and SAXS (on the right) patterns of a doubly oriented PE film. Incident X-ray beams are parallel to the X_1-, X_2- and X_3-axes. The WAXS in (c) shows that the *b*-axis is parallel to X_2. The WAXS in (b) shows that the *a*-axis is tilted by $\psi = 8°$ against the $\{X_1 X_2\}$ plane around the *b*-axis, so that the elongated four-point reflections in the SAXS in (b) tilt somewhat to the radial direction.

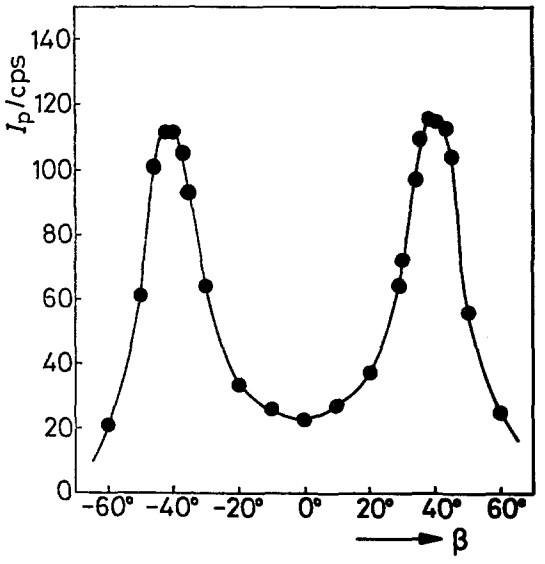

Figure 8 The variation of the peak intensity of the SAXS reflection for the doubly oriented PE film when the film was rotated around the X_3-axis. The rotation angle β is taken to be zero when the incident X-ray beam is parallel to the X_1-axis (see Fig. 1). The reflection has maximum intensities at $\beta = \pm 40°$.

shown schematically in the projection on the $\{X_1X_2\}$ plane. When the angle of γ deviates from τ_a, the tangential points of the Ewald sphere to the contour lines (marked by black spots) or the In the X_3 pattern of Fig. 7 one can see weak 1 1 0 reflections also in the horizontal X_1-direction. These are obviously produced by mPCs which lie in the middle of the specimen film and are therefore not exposed to the plane stress field on the two surfaces.

The SAXS pattern in the X_2-direction shows a four-point diagram, so that the lamellae surfaces are inclined around the b-axis by an angle $\phi = 40°$ from the $\{X_1X_2\}$ plane. These long spacing peaks are very diffuse in the X_1-direction and hence have an intensity bridge between them. The SAXS pattern in the X_1-direction therefore has a meridional two-point diagram. This can be explained by the statistical fluctuation of the macrolattice consisting of centres of microparacrystals according to the paracrystalline theory, because the line broadening of SAXS reflections depends mainly on the paracrystalline superlattice factors. The X_3 fluctuation of the positions of the mPCs is much larger between lateral adjacent mPCs of the same lamella than those of neighbouring mPCs in an ultrafibril [15], so that the unidirectional SAXS reflections are elongated in the

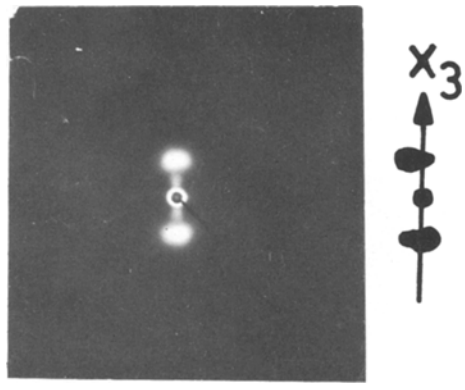

Figure 9 SAXS photographs in X_1-direction for the doubly oriented film at $\beta = 40°$ in Fig. 8. The reflection is asymmetric with respect to the X_3-axis.

direction normal to the microfibrils and have a broad intensity distribution in this direction.

The distribution in the X_1-direction can be measured quantitatively if the sample film is rotated around the X_2-axis with the incident X-ray beam parallel to the X_1-axis. The result is shown in Fig. 8; the distribution curve now has maxima at rotation angles $\phi = \pm 40°$. Here again it was confirmed that lamellar surfaces are inclined by $\phi \neq 0°$. Fig. 9 shows the SAXS pattern when $\phi = 40°$; the meridional reflections are much stronger compared with those at the usual position (Fig. 7a) and the intensity ratio is >5 as can be seen from Fig. 8.

As mentioned above, the c-axis of microparacrystals tilts around the b-axis by $\psi = 8°$ from the X_3-axis. The lamellar basal surface which gives a four-point SAXS diagram therefore inclines by $\phi \pm \psi = 32°$ or $48°$ from the $\{0\,0\,1\}$ netplane. One can distinguish between these two possibilities from the shape of the four-point SAXS reflections. If the elongated reflections are tilted to the radial direction (parallel to the c-axis), then the inclination angle should be $\phi + \psi$, whereas if they are tilted to the tangential direction (orthogonal to the c-axis) it should be $\phi - \psi$. As seen from Fig. 7b the four-point reflections are somewhat tilted to the radial direction, so that the angle between the normal to the microparacrystal lamellar surfaces and the chain axis is $\phi + \psi = 48°$ (Figs. 9 and 10).

In the experiment of Fig. 8, the dependence of the long period on the rotation angle β was also measured. Fig. 11 shows the result; the long period decreases with increasing β and suddenly levels off at $\beta = \phi$. To understand this result one has to analyse the SAXS diagram two-dimensionally.

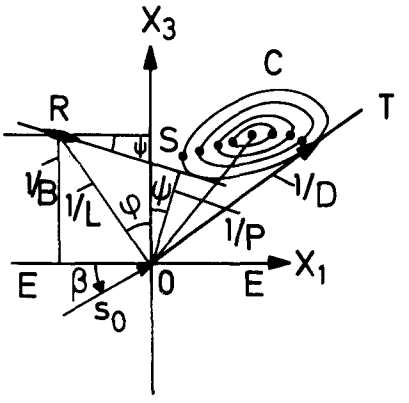

Figure 10 Schematic SAXS intensity profile projected on the $\{X_1X_3\}$ plane for the doubly oriented PE film. See text for notation.

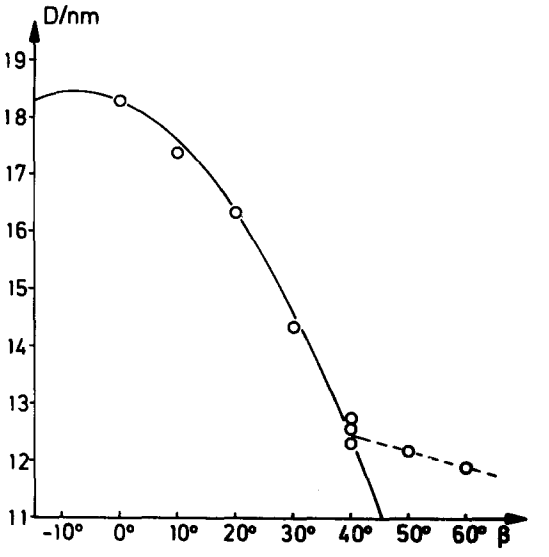

Figure 11 The variation of the Bragg distance D due to the meridional two-point reflections by β-rotation (see Figs. 8 and 10). Solid curve above the calculated values from Equation 4; circles show observed ones. For $|\beta| > 40°$, D decreases much more slowly with increasing β as a consequence of the rangential construction to the contour lines of the reflection profile C in Fig. 10.

The angle β in Fig. 11 is given in Fig. 10 by the angle between the direction S_0 of the incident X-rays and the equator E along the X_1-axis. For $\beta = \psi$ the Ewald sphere goes to OR and the distance D of the small angle reflection in Fig. 9 is given by the periodicity L of the lamellae, $L = 12.5$ nm. For $\beta = -\psi$ the Ewald sphere goes to OS and D has its maximum value $D_{max} = P = 18.4$ nm where P is the periodicity along the microfibrils (Fig. 14). For all other β-values one obtains

$$D = P\cos(\beta + \psi) \qquad (7)$$

This function of D versus β is plotted in Fig. 11 as a full line and agrees satisfactorily with the observed positions of the maximum of the SAXS reflection until $\beta = 40°$. For higher β-values D decreases much more slowly compared with the theoretical curve. This can be easily explained by the intensity distribution of the reflection C, schematically drawn in Fig. 10. The end of the reciprocal vector $1/D$ is given by the point where it touches the contour lines as a tangent. The black points represent these tangential points. They lie on a straight line like RS for the reflection R on the left side until the maximum intensity of C, but after that describe a curve which explains the deviation of the observed values in Fig. 11 from Equation 4.

We have suppressed until now the fact that the four-point SAXS reflections do not lie exactly in a $\{X_1X_3\}$ plane. Remembering that the larger sides of the microparacrystals are parallel to the $\{\bar{3}\,1\,0\}$ planes and tilt by $\tau_a = 26°$ from the macroscopic film surface or a $\{X_2X_3\}$ plane, it is expected that the SAXS reflections lie orthogonal to the $\{3\,1\,1\}$ netplanes. In fact the angle between the $\{3\,1\,1\}$ and $\{0\,0\,1\}$ netplanes is 48.9° and agrees well with the observed value of 48°. This assignment was also supported from other experiments. The two-point reflections in the SAXS diagram at $\beta = 40°$ (Fig. 9) are not exactly mirror-symmetric to the X_3-axis, but oval. The centres of the SAXS reflections are therefore somewhat removed from the X_1X_3 plane. To prove this in more detail, the sample was rotated around the X_3-axis successively by an angle γ. Fig. 12 shows the result; at $\gamma = 0$ the X-ray beam is in the X_2-direction as in Fig. 7b and at $\gamma = 90°$ it appears as in Fig. 7a. One can see that at $\gamma \cong \gamma_a \sim 20°$ to 30° one pair of diagonal reflections has a maximum intensity and the intensity of the other pair becomes much weaker, because it is remote by $2\gamma_a$ from the Ewald sphere (Fig. 13). It is interesting to note that $\gamma_a \sim \tau_a$ (see Fig. 3). The orientation of the cigar-shaped mPCs defines the direction in the X_1X_2 plane of steepest inclination ($\beta = 40°$) of the lamellae surfaces. The long axes of the mPCs are therefore orthogonal to X_3 and the $\beta = 40°$ inclination of the lamellae to the X_1X_2 plane is orthogonal to their long axes. Another observation from Fig. 12 is that the distance of the SAXS peak from the primary beam has a maximum at $\gamma = \tau_a$. In Fig. 13 the intensity distribution of the reciprocal lattice points is

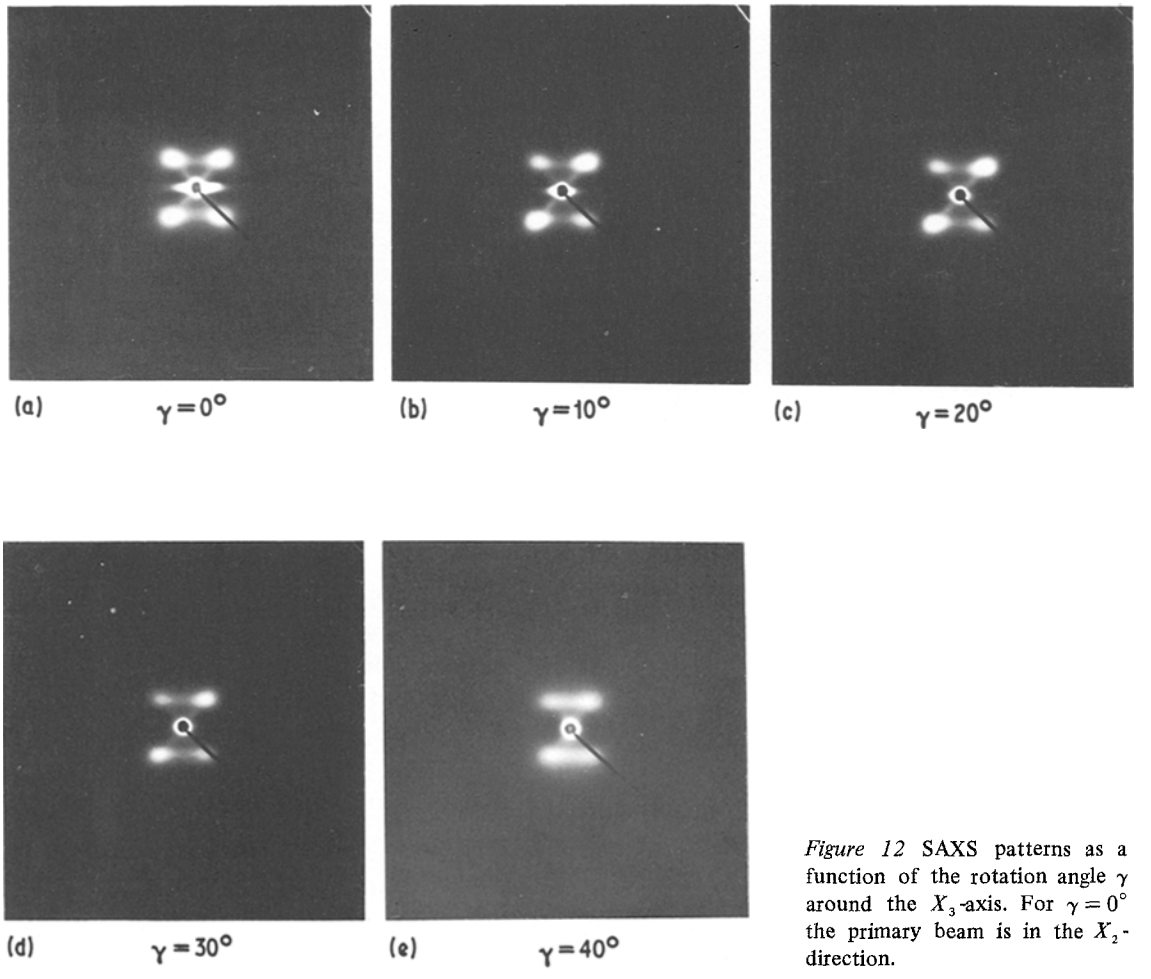

Figure 12 SAXS patterns as a function of the rotation angle γ around the X_3-axis. For $\gamma = 0°$ the primary beam is in the X_2-direction.

positions of the two-point diagonal reflections shift slightly to the centre of the SAXS pattern and the intensity decreases.

Following a similar argument, the micropara-crystallite basal surfaces for the uniaxially oriented sample should be {5 2 3} netplanes since the angle between the {5 2 3} and {0 0 1} netplanes is 34°, and agrees well with the value of 35° obtained from the four-point SAXS pattern. The {2 0 1} planes are also inclined at 35° to the {0 0 1} net-plane, as reported by Keller and Sawada [1] for the spherulites of linear PE crystallized at high temperature, but in this case one cannot explain the {5 2 0} netplanes of the larger lateral sides of the crystallites.

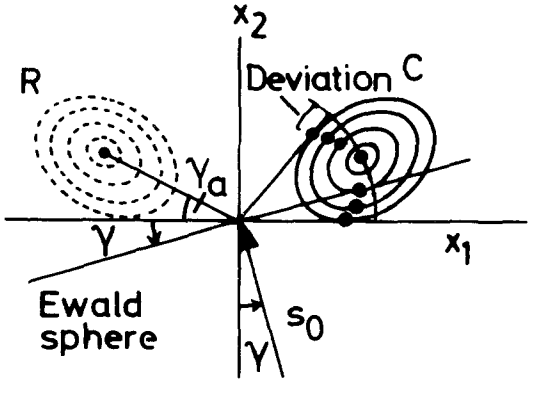

Figure 13 Explanation of the shift of the SAXS reflections observed in Fig. 12 as a function of γ. The points give the position of the intensity peak.

6. Central continuous scattering in SAXS patterns

As seen in Figs. 4 and 7 the SAXS patterns in the X_2- and X_3-directions show central continuous scattering for both uniaxially and doubly oriented samples. The continuous scattering runs in the direction normal to the film surface of the sample. If this scattering is due to "total reflection", it will disappear when the sample film is rotated above the critical angle of PE around the X_3-axis.

The critical angle θ_c is given by

$$\theta_c = \sqrt{2\delta}; \quad \delta = 6.423 \times 10^{-6} Z\rho/M \quad (8)$$

for Cu$K\alpha$ radiation. Here Z is the number of electrons in the monomeric unit, M is the molar mass of the monomeric unit, and ρ is the density in $Mg\,m^{-3}$. The value for PE is $\theta_c = 9'$. As seen from Fig. 12, the central continuous scattering does not disappear when the rotation angle γ around the X_3-axis exceeds the critical angle. Therefore the central continuous scattering for this sample is due to the voids in the sample. They must have the shape of fissures parallel to the macroscopic film surface $\{X_2X_3\}$ since the central continuous scattering consists of streaks in the direction perpendicular to the film surface of the sample and decreases rapidly within a few degrees and almost disappears above 20°.

7. Discussion

The combined SAXS and WAXS analysis of the doubly oriented PE films shows that the SAXS pattern does not only depend on the orientation and periodicity of the bundles of lamellae, but also on the direction of the chain molecules, which are tilted by $\psi = 8°$ to the stretching direction. In Fig. 7b one could also observe that the SAXS reflection is tilted somewhat to the radial direction and not orthogonal to X_3 or parallel to X_1 which leads to Equation 7 and Fig. 11. How is it possible that SAXS is influenced by the orientation of chain molecules? This interesting question might be answered conventionally as follows: the inclination angle ψ of the chains (Fig. 14) is detectable, if the bundle of the lamellae has plane lateral sides parallel to the chains. Then according to Fig. 14 the diffraction pattern is explained in the conventional way by the convolution product of the shape of one lamella (all lamellae have the same shape) with a one-dimensional point lattice function (PF), each point the centre of one lamella. Its Fourier transform is the product of the transform of the lamella shape (LS) and a set of equidistant lines (EL) orthogonal to the direction of the point row (Fig. 14). Now it is clear from electron micrographs that such bundles with identical lamella shapes do not exist. This conventional explanation is therefore unacceptable. Our explanation is that the bundles have arbitrary shapes, but the lamellae consist of discrete mPCs. The single microparacrystallites are arranged nematic-like with a distance statistic $H_3(x)$ between

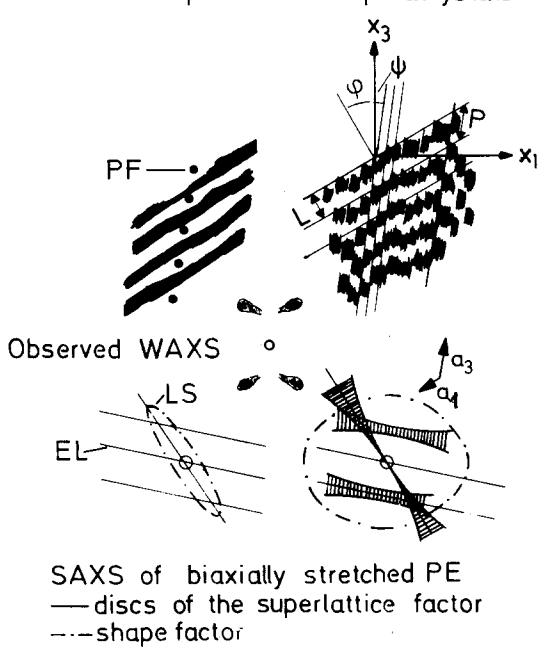

Figure 14 Fibrillar and lamellar features of the superstructure of the doubly oriented PE film deduced from the SAXS pattern of Fig. 7 (see the text for details).

the centres of adjacent microparacrystallites in the chain direction and a statistic $H_1(x)$ between the centres of neighbouring mPCs in the direction parallel to the lamellar basal plane (Fig. 15). The lattice factor $Z(b)$ of this paracrystalline superlattice is, according to the theory of paracrystals [8], the product of two disc-like equidistant sets, the one orthogonal to $\mathbf{a}_3$, the other orthogonal to

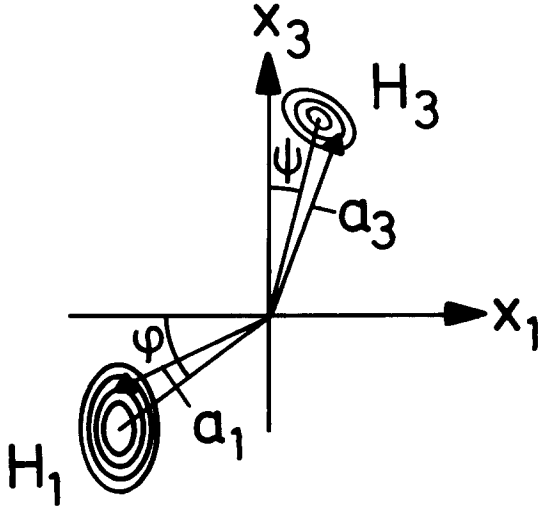

Figure 15 Coordination statistics $H_1(x)$ and $H_2(x)$ of the paracrystalline superlattice of the microparacrystallites.

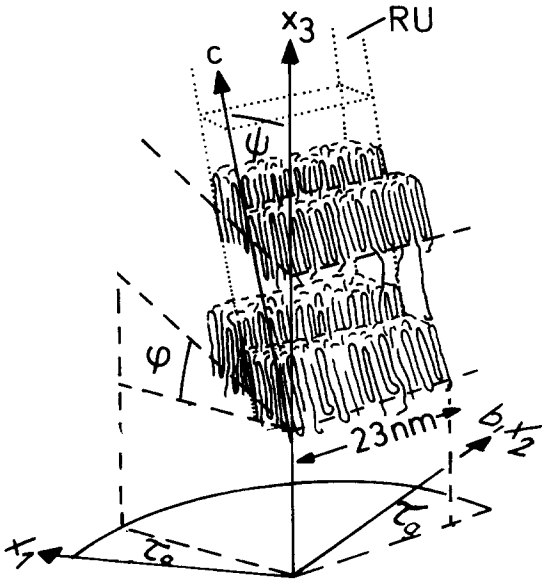

Figure 16 A ribbon-like ultrafibril (RU) of biaxial oriented PE with 23 nm long mPCs; the long axis is parallel to the $\{X_1X_2\}$ plane and arranged in lamellar-like layers which are tilted by 40° against $\{X_1X_2\}$. The gradient of this slope is turned by $\tau_a = 26°$ from the X_1-axis. The rhombohedric lattice cell has a *b*-axis parallel to X_2. The *c*-axis is turned around it by $\psi = 8°$ from X_3.

$\mathbf{a}_1$. The SAXS reflection is then given by the Miller indices $(h_1h_3) = (0\,1)$ as described in Fig. 14 on the right hand side. Fig. 10 gives the plate-like intensity distribution of one diagonal reflection C in the reciprocal space in the $\{X_1X_3\}$ plane. The mean vector $\mathbf{a}_3$ of H_3 is given by the reciprocal value of OS. On the line RS therefore lie all reflections $h\,0\,1$. The line OR, on the other hand, represents all reflections $0\,0\,l$ and is orthogonal to $\mathbf{a}_1$. The reflection R, as the intersection of both lines, therefore has the indices (0 0 1) in the paracrystalline superstructure which has monoclinic lattice cells. Its above mentioned plate-like shape comes from the fact that the fluctuation widths of $\mathbf{a}_3$ in the X_3-direction is smaller than that of $\mathbf{a}_1$ in the direction of the normal to the lamellae.

The important and fundamental consequence is that the SAXS pattern gives direct informations of statistical fibrillar-like correlations between adjacent lamellae. The fold surfaces of the lamellae are therefore not plane, but show statistical irregularities which are mutually correlated in the direction of the chains with the neighbouring surfaces, as drawn schematically in Fig. 14. This means, from the physical point of view, that tie-molecules transfer statistical correlations of the lamellar surfaces to the next lamella, mostly in the chain direction. The SAXS pattern therefore indicates ultrafibrillar structure elements of lamellar bundles. Both, lamellar and ultrafibrillar features are represented in the superstructures. The conventional theory of mesophases can never combine such structure elements to an entity [16]. The theory of paracrystals gives the most convenient way of explaining these statistical correlations between the lamellae by introducing microparacrystals, which were established by WAXS measurements, and a paracrystallite superlattice, whose cell edges interconnect the centres of the mPCs (Figs. 14 and 15). Fig. 16 is a schematic perspective drawing of the structure of biaxially oriented PE.

Acknowledgements

One of the authors (KK) gratefully acknowledges the invaluable suggestions and discussions of Professor Emeritus I. Sakurada of Kyoto University. Most of the experiments in this work were carried out in the Central Research Institute of Kuraray Co. Ltd. with the generous support of Dr A. Yasui, Director of the Institute, to whom the authors are greatly indebted, and KK also would like to thank Dr Y. Tanaka from this institute for the help which he has given.

The authors wish to express special appreciation to Dr J. Laboda-Čačković and Dr H. Čačković of the Fritz-Haber-Institut der Max Planck-Gesellschaft for the helpful discussions, and to Dr W. Vogel and Dr J. Haase of this institute for the help in the crystallite size determination.

References

1. A. KELLER and S. SAWADA, *Makromol. Chem.* 74 (1964) 190.
2. J. LOBODA-ČAČKOVIĆ, H. ČAČKOVIĆ and R. HOSEMANN, *J. Polymer Sci. C* **42** (1973) 577.
3. I. L. HAY and A. KELLER, *J. Mater. Sci.* **1** (1966) 41.
4. *Idem, ibid* **2** (1967) 538.
5. R. BONART and R. HOSEMANN, *Kolloid-Z. u. Z. Polymere* **186** (1962) 16.
6. W. WILKE, W. VOGEL and R. HOSEMANN, *ibid* **237** (1970) 317.
7. A. SCHÖNFELD. W. WILKE, G. HÖHNE and R. HOSEMANN, *ibid* **250** (1972) 102.
8. R. HOSEMANN and S. N. BAGCHI, "Direct Analysis of Diffraction by Matter", (North-Holland, Amsterdam, 1962).
9. W. PECHHOLD, S. BLASENBREY and S. WOERNER, *Kolloid-Z. u. Z. Polymere* **189**, (1963) 14.

10. K. KAJI, *Makromol. Chem.* **175** (1974) 311.
11. A. H. WINDLE, *J. Mater. Sci.* **10** (1975) 252.
12. A. SCHÖNFELD and W. WILKE, *Kolloid-Z. u. Z. Polymere* **250** (1972) 496.
13. C. W. BUNN, *Trans. Faraday Soc.* **35** (1939) 482.
14. G. ALLEN, G. GEE and G. J. WILSON, *Polymer* **1** (1960) 456.
15. R. BONART and R. HOSEMANN, *Makromol. Chem.* **39** (1960) 105.
16. C. HERMANS, *Z. Krist* **79** (1931) 186.

Received 12 May and accepted 2 August 1977.